Structure

Article

The respiratory supercomplex from *C. glutamicum*

Graphical abstract

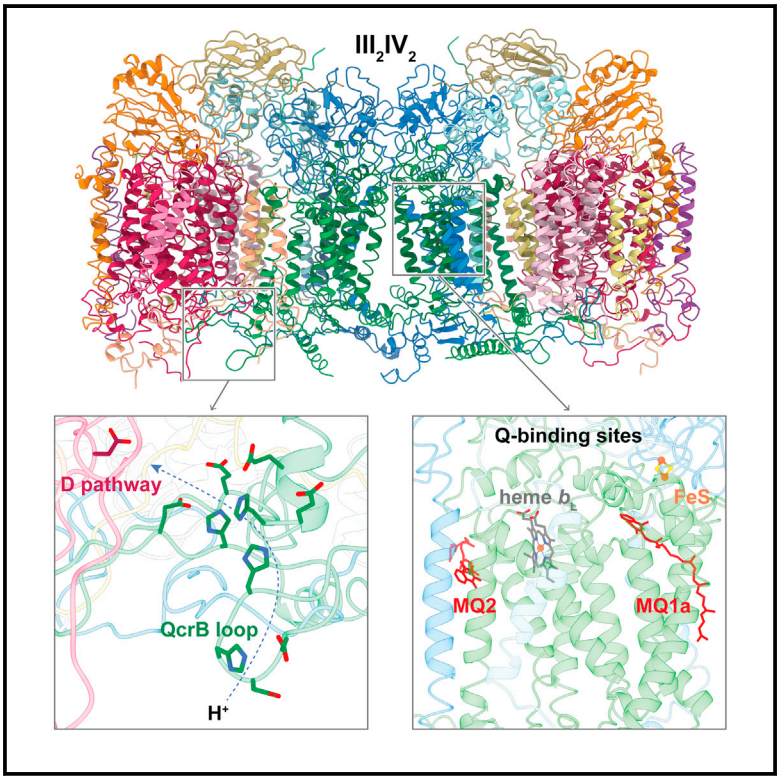

Authors

Agnes Moe, Terezia Kovalova, Sylwia Król, ..., John L. Rubinstein, Martin Högbom, Peter Brzezinski

Correspondence

john.rubinstein@utoronto.ca (J.L.R.), martin.hogbom@dbb.su.se (M.H.), peter.brzezinski@dbb.su.se (P.B.)

In brief

Moe et al. report a structure of the major energy-conserving membrane-bound protein complex in *C. glutamicum*, a supercomplex composed of respiratory complexes III and IV. The structure reveals the position and structure of quinone-binding sites, the electronic connection between the components as well as proton pathways.

Highlights

- Structure is determined of the *C. glutamicum* respiratory supercomplex at 2.9 Å resolution
- Menaquinone binding sites are resolved
- A di-heme cyt. *cc* subunit electronically connects complexes III and IV
- A proton pathway in CIV is defined by a sub-structure of CIII at the cytoplasmic side

Moe et al., 2022, Structure *30*, 338–349
March 3, 2022
https://doi.org/10.1016/j.str.2021.11.008

CellPress

CellPress
OPEN ACCESS

Structure

Article

The respiratory supercomplex from *C. glutamicum*

Agnes Moe,[1,6] Terezia Kovalova,[1,6] Sylwia Król,[1] David J. Yanofsky,[2,3] Michael Bott,[4] Dan Sjöstrand,[1] John L. Rubinstein,[2,3,5,*] Martin Högbom,[1,*] and Peter Brzezinski[1,7,*]

[1]Department of Biochemistry and Biophysics, The Arrhenius Laboratories for Natural Sciences, Stockholm University, 106 91 Stockholm, Sweden
[2]Molecular Medicine Program, The Hospital for Sick Children, 686 Bay Street, Toronto, ON M5G 0A4, Canada
[3]Department of Medical Biophysics, The University of Toronto, 101 College Street, Toronto, ON M5G 1L7, Canada
[4]Institute of Bio- and Geosciences, IBG-1: Biotechnology, Forschungszentrum Jülich, 52425 Jülich, Germany
[5]Department of Biochemistry, The University of Toronto, 1 Kings College Circle, Toronto, ON M5S 1A8, Canada
[6]These authors contributed equally
[7]Lead contact
*Correspondence: john.rubinstein@utoronto.ca (J.L.R.), martin.hogbom@dbb.su.se (M.H.), peter.brzezinski@dbb.su.se (P.B.)
https://doi.org/10.1016/j.str.2021.11.008

SUMMARY

Corynebacterium glutamicum is a preferentially aerobic gram-positive bacterium belonging to the phylum Actinobacteria, which also includes the pathogen *Mycobacterium tuberculosis*. In these bacteria, respiratory complexes III and IV form a $CIII_2CIV_2$ supercomplex that catalyzes oxidation of menaquinol and reduction of dioxygen to water. We isolated the *C. glutamicum* supercomplex and used cryo-EM to determine its structure at 2.9 Å resolution. The structure shows a central $CIII_2$ dimer flanked by a CIV on two sides. A menaquinone is bound in each of the Q_N and Q_P sites in each CIII and an additional menaquinone is positioned ~14 Å from heme b_L. A di-heme cyt. *cc* subunit electronically connects each CIII with an adjacent CIV, with the Rieske iron-sulfur protein positioned with the iron near heme b_L. Multiple subunits interact to form a convoluted sub-structure at the cytoplasmic side of the supercomplex, which defines a path for proton transfer into CIV.

INTRODUCTION

In the final steps of energy conversion in aerobic organisms, electrons are transferred through the respiratory chain, which consists of membrane-bound proteins that transfer electrons from donors, such as NADH, to the final electron acceptor, O_2. This electron current drives proton translocation from the negative (*n*) to the positive (*p*) side of the membrane, thereby maintaining a voltage difference and a proton concentration gradient that together generate a transmembrane proton motive force (PMF). The free energy stored in the PMF is used by ATP synthase for production of ATP from ADP and phosphate, or to drive transmembrane transport.

NADH dehydrogenases and other enzymes transfer electrons to membrane-soluble quinone (Q), reducing it to quinol (QH_2). In mitochondria and many bacteria, the reduced QH_2 donates electrons to the cyt. bc_1 complex, also known as complex III, which is found as an obligate dimer ($CIII_2$). In each monomer of $CIII_2$ the QH_2 binds at the Q_P site, near the *p* side of the membrane. Energy conservation is realized through a bifurcated electron transfer from QH_2, referred to as the Q-cycle (Mitchell, 1976) (Figure 1). The first electron from QH_2 is transferred along the so-called C branch to a Rieske iron-sulfur protein, which harbors a redox-active 2Fe-2S (FeS) center. Oxidation of QH_2 leads to the release of two protons to the *p* side of the membrane. The second electron is transferred along the B branch, passing electrons sequentially to the low-potential heme b_L and the high-potential heme b_H before reducing Q bound in a second site, the Q_N site, located near the *n* side of the membrane. In canonical $CIII_2$ the FeS center, which is bound in a mobile ectodomain, receives the electron from QH_2 while in its B position in proximity to heme b_L. Upon reduction of the FeS center and heme b_L, the mobile FeS domain rotates by ~60° toward the *p* side to adopt its C position near cyt. c_1. In the C position, the electron from FeS is transferred first to heme c_1 and then to a water-soluble cyt. *c* (Zhang et al., 1998) (Figure 1). Cyt. *c* donates electrons to the last component of the respiratory chain, cytochrome *c* oxidase (also known as cyt. aa_3 or complex IV, CIV). After exchange of Q for QH_2 at the Q_P site of CIII, the sequence of events is repeated, resulting in formation of QH_2 at the Q_N site and abstraction of two protons from the *n* side of the membrane, contributing further to the PMF (for review, see Berry et al., 2013; Brzezinski et al., 2021; Cramer et al., 2011; Crofts, 2004; Mulkidjanian, 2005; Sarewicz and Osyczka, 2015; Sarewicz et al., 2021; Crofts, 2021).

The primary electron acceptor from cyt. *c* in CIV is a di-nuclear copper A site, Cu_A, on the *p* side of the membrane. This copper center transfers electrons to heme *a*, which then transfers the electron to the binuclear catalytic site composed of a heme a_3 and copper Cu_B. Upon electron transfer to the catalytic site, heme a_3 binds an O_2 molecule, which is reduced to H_2O, in a process linked to proton uptake from the *n* side of the membrane (Figure 1). The free energy released upon oxidation of cyt. *c*

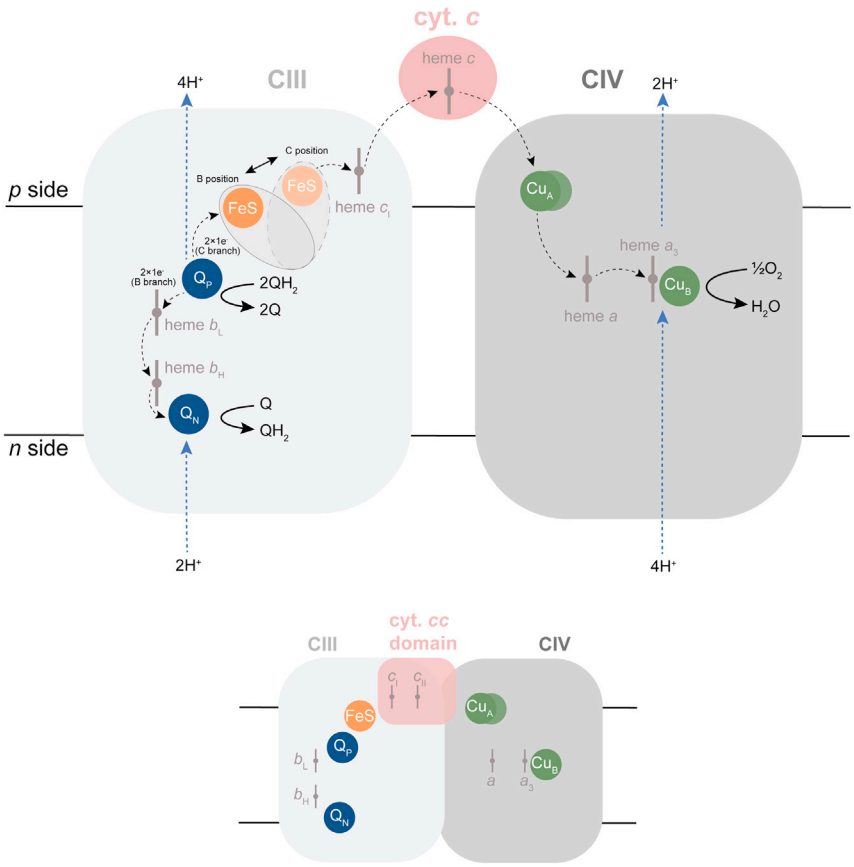

Figure 1. Reactions catalyzed by CIII and CIV

Upon binding of QH_2 at the Q_P site in CIII, one electron is transferred to FeS, along the C branch, and one along the B branch, via hemes b_L and b_H to the Q at the Q_N site. The reaction sequence is repeated upon binding of a second QH_2 at the Q_P site. In canonical CIII, the mobile FeS ectodomain moves from the electron-receiving B position to the electron-donating C position to transfer an electron to cyt. c_1, which reduces water-soluble cyt. *c*. Oxidation of QH_2 at the Q_P site is associated with proton release to the *p* side of the membrane while reduction of Q at the Q_N site is associated with proton uptake from the *n* side. Reduced cyt. *c* transfers electrons to Cu_A, heme *a*, and the heme a_3/Cu_B catalytic site of CIV where O_2 is reduced to H_2O. Each electron transfer from cyt. *c* to the catalytic site is linked to pumping of one proton across the membrane. The lower part of the figure shows the *M. smegmatis* III_2IV_2 supercomplex where electrons are transferred from CIII to CIV via a di-heme cyt. *cc* domain.

and reduction of O_2 is conserved by proton pumping from the *n* to the *p* side of the membrane (for review, see Brzezinski and Gennis, 2008; Hosler et al., 2006; Wikström et al., 2015).

Three major CIV families have been defined on the basis of amino acid sequences as well as functionally important structural features such as proton pathways (Hemp and Gennis, 2008; Lee et al., 2012; Pereira et al., 2001). Class A1 members are characterized by an XGHPEVY motif in subunit I and comprises the mitochondrial and many bacterial CIVs, including the enzyme from *Corynebacterium glutamicum*. In the XGHPEVY motif, H is a ligand of Cu_B (His265, *C. glutamicum* CIV numbering) while Y (Tyr269) is covalently linked to His265 (Iwata et al., 1995; Qin et al., 2006; Svensson-Ek et al., 2002; Tsukihara et al., 1996). The A-type bacterial CIVs harbor two proton pathways, denoted D and K, used for proton uptake from the *n* side of the membrane (Iwata et al., 1995; Qin et al., 2006; Svensson-Ek et al., 2002; Tsukihara et al., 1996). The K pathway transfers two protons to the catalytic site upon reduction of heme a_3 and Cu_B, while the D pathway transfers two protons to the catalytic site after binding of O_2 to heme a_3 and for all protons that are pumped across the membrane (Brzezinski and Ädelroth, 1998; Konstantinov et al., 1997; Sharma and Wikström, 2016; Ädelroth et al., 1997, 1998). A third, H pathway, was proposed to be involved in proton pumping in the mammalian CIV (Yoshikawa and Shimada, 2015), but it is presumably not found in bacterial CIV (Lee et al., 2000).

Gram-positive bacteria of the phylum Actinobacterium do not harbor genes for a water-soluble cyt. *c* (Bott and Niebisch, 2003) and the series of events that allow a Q-cycle in CIII is not well understood. As seen in *Mycobacterium smegmatis* (Gong et al., 2018; Megehee et al., 2006; Wiseman et al., 2018; Yanofsky et al., 2021) and *C. glutamicum* (Graf et al., 2016; Kao et al., 2016; Niebisch and Bott, 2001, 2003; Sone et al., 2001), Actinobacterial $CIII_2$ and CIV form an obligate $CIII_2CIV_2$ supercomplex in which electron transfer between CIII and CIV is mediated by a di-heme cyt. *cc* domain that replaces both cyt. c_1 of the canonical $CIII_2$ and the water-soluble cyt. *c* (Figure 1, lower part).

Assembly and maturation of the $CIII_2CIV_2$ supercomplex in Actinobacteria is poorly understood, but a few proteins involved in copper and heme *a* insertion into CIV have recently been identified in *C. glutamicum* (Davoudi et al., 2019; Morosov et al., 2018). *C. glutamicum* was isolated in 1957 in Japan during a search for glutamate-excreting bacteria (Kinoshita et al., 1957) and has become a model organism in industrial biotechnology. It is of vast economic importance because strains of the species are used for production of amino acids, in particular L-glutamate (about 3 million tons per year) and L-lysine (about 2 million tons per year). Monosodium glutamate is used as food additive, as it elicits the umami taste (Hashimoto, 2017). L-Lysine is used as an additive for animal feed that is often limited in some essential amino acids (Eggeling and Bott, 2015). Industrial L-glutamate and L-lysine production are aerobic processes dependent on a functional respiratory chain and in particular on a functional $CIII_2CIV_2$ supercomplex, which is the major energy-conserving complex in *C. glutamicum* with its absence causing a severe growth defect (Davoudi et al., 2019).

In order to gain insight into electron transfer and proton translocation in the *C. glutamicum* $CIII_2CIV_2$ supercomplex, we determined its high-resolution cryo-EM structure. The structure shows density for a menaquinone (MQ) bound in each of the Q_N and Q_P sites of each CIII monomer. In addition, an MQ was

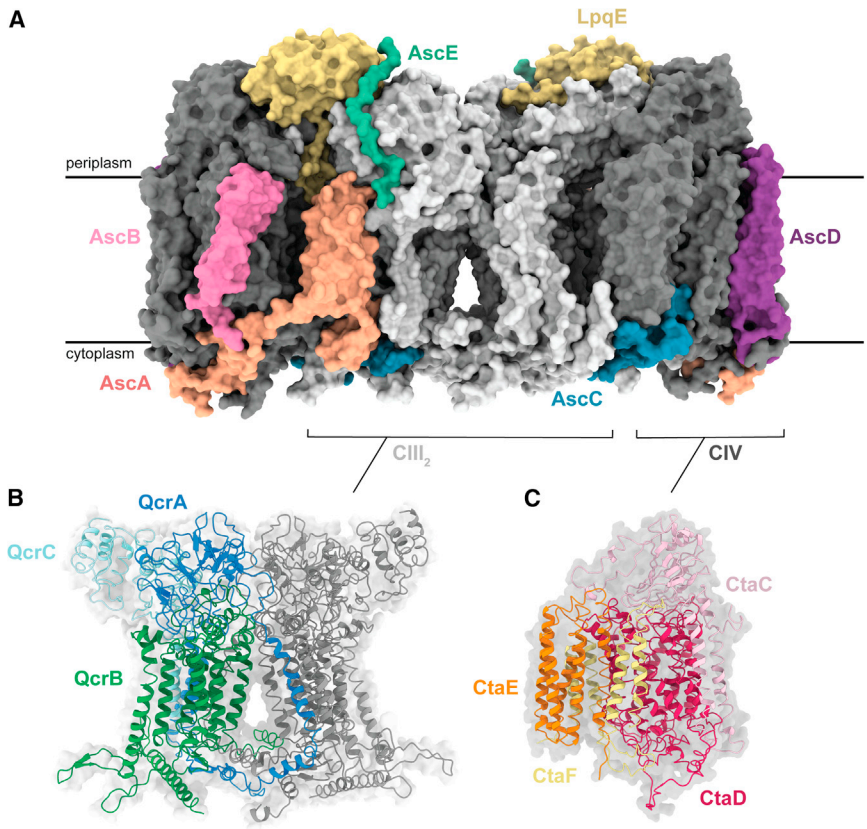

Figure 2. Structure of the supercomplex

(A and B) (A) The entire III_2IV_2 supercomplex with core subunits in light ($CIII_2$) or dark (CIV) gray, and accessory subunits in color as indicated. (B) The complex III_2 dimer in which each monomer is composed of subunits QcrA-C. The right-hand side monomer is shown in gray while the subunits of the left-hand side monomer are colored. Note that TMH 1 of QcrA is integrated into the other half of the dimer. A surface representation of the entire $CIII_2$ is shown in light gray.

(C) The core of complex IV with CtaC-F, shown in color and a surface representation of the entire CIV in dark gray.

found in a newly identified site on the membrane *p* side, ~14 Å from heme b_L. As with the *M. smegmatis* supercomplex (Wiseman et al., 2018; Yanofsky et al., 2021), an extended loop of the QcrB subunit covers the cytoplasmic opening of the D proton pathway of CIV, defining a proton-entry route via protonatable residues of QcrB. The FeS ectodomain in $CIII_2$ was found to be locked in the B position, which suggests a Q-cycle mechanism that is gated only by local proton transfer rather than by FeS movement.

RESULTS AND DISCUSSION

Isolation of the supercomplex

The 750-kDa *C. glutamicum* $CIII_2CIV_2$ supercomplex was purified using a Strep-tag on the CtaD subunit of CIV (Niebisch and Bott, 2003) (Figure S1 and Table S1; Altschul et al., 1990). Absorbance difference spectroscopy suggests a heme *a*:*b*:*c* ratio of approximately 1:1:1, consistent with the $CIII_2CIV_2$ composition of the supercomplex (Kao et al., 2016; Niebisch and Bott, 2003). Mass spectrometry identified all of the subunits of CIII (QcrA, QcrB, QcrC) and CIV (CtaC, CtaD, CtaF), except for CtaE, which is a hydrophobic membrane protein that is likely difficult to detect by mass spectrometry (Table S2), as seen with the equivalent subunit in *M. smegmatis* (Wiseman et al., 2018) and Cox3, which is equivalent to CtaE and CtaF in *Saccharomyces cerevisiae* (Hartley et al., 2019). Three proteins identified previously to be associated with the $CIII_2CIV_2$ supercomplex (Niebisch and Bott, 2003) were detected by mass spectrometry: P20 (later renamed to PRSAF1), P24, and P29 (later renamed to LpqE), with PRSAF1 and LpqE subsequently modeled in the structure. Two previously unidentified proteins were detected by mass spectrometry: Cg0935 and Cg1128, with Cg0935 subsequently modeled in the structure. The MQH_2:O_2 oxidoreductase activity of the supercomplex was ~100 ± 10 e^-/s^{-1} (±SD, four technical replicates), consistent with earlier measurements (Graf et al., 2016; Niebisch and Bott, 2003).

Overall structure of the supercomplex

To understand the mechanism by which the *C. glutamicum* III_2IV_2 supercomplex links electron transfer to proton translocation, we determined its structure by cryo-EM to a nominal resolution of 2.9 Å (Figures S2, S3, and Table S3). Proteins identified in the *C. glutamicum* respiratory supercomplex structure are summarized in Table S1. The map shows that the core of the supercomplex is composed of a $CIII_2$ dimer flanked by two distal CIV monomers (Figure 2A). This overall arrangement and its geometry are the same as in the *M. smegmatis* supercomplex (Gong et al., 2018; Wiseman et al., 2018; Yanofsky et al., 2021). Each protomer of $CIII_2$ is composed of three subunits, QcrA-C (Figure 2B) while the core of CIV is composed of four subunits, CtaC-F (Figure 2C) (Bott and Niebisch, 2003; Kao et al., 2016). An additional six subunits were identified in the *C. glutamicum* supercomplex structure (Figure 2A), two of which (LpqE and PRSAF1) were identified previously in *C. glutamicum* (Niebisch and Bott, 2003) and are also found in the *M. smegmatis* supercomplex structure (Gong et al., 2018).

We propose a new unifying nomenclature and refer to these additional subunits as AscX (Actinobacterial supercomplex, subunit X), except for LpqE (P29), which is an established name (where applicable, the previously used names are given below in parentheses). The map allowed for construction of an atomic model (Liebschner et al., 2019) for all subunits except for AscD and AscE (Figure S4 and Table S3), which could not be identified. On the periplasmic side of the supercomplex subunit LpqE is attached to the membrane via an N-terminal lipid anchor (Figure 2A, colored in yellow). It also interacts with the cyt. *cc* domain of QcrC, and subunits QcrA, CtaC, and CtaD. As shown previously, LpqE did not co-purify with CIII or CIV alone, suggesting

that the interaction with QcrC, which is absent in both individual complexes, is necessary for the presence of LpqE. Subunit AscA (colored in light orange) is attached to both $CIII_2$ and CIV. The N-terminal part of the protein starts with a short loop that continues to form two transmembrane α-helices attached to subunit QcrB of $CIII_2$. A loop formed by 54 residues near the C terminus of AscA interacts with a loop of CtaD, and the two transmembrane α-helices. Like LpqE, AscA was not co-purified with the isolated CIII and CIV complexes, indicating that interaction with both QcrB and CtaD is required for co-purification.

A ~63-residue stretch of protein was identified in the map (labeled AscB and colored pink). A tentative sequence was modeled based on the density and used to search the NCBI (ncbi.nlm.nih.gov) database for potential matches. This search identified protein GenBank: Cg0775, which provides a convincing representation of the complete density (Figure S4B), although this protein was not identified from the mass spectrometry analysis. The putative AscB subunit is folded into a transmembrane α-helical hairpin that is attached to CtaD. A short peripheral protein chain, composed of 63 amino acid residues, was identified as AscC (Cg0935, colored in blue) by mass spectrometric analysis (Figure S4B). AscC is partially attached to QcrB on the cytoplasmic side of the supercomplex. The protein chain extends to contact CtaE and CtaF, as well as a QcrB loop that covers one of the proton pathways of CIV (see below). AscD (colored in purple) forms a transmembrane α-helical hairpin that is a part of CIV. It is located between the membrane-facing CtaF α-helical hairpin and CtaC α-helical hairpin. However, the sequence for AscD could not be registered in the experimental density. The N- and C-terminal loops of AscD are also part of a cytoplasmic side sub-structure, discussed in more detail below. AscE (colored in green) is attached to the FeS domain of QcrA and to LpqE. The resolution of this part of the structure is low and it was therefore modeled as polyalanine. The density also shows a similar lipid anchor to that of LpqE. In the first description of the supercomplex, another accessory protein (P24, Cg2444) was co-purified with the QcrAB complex; however, it was not present in all preparations of the supercomplex (Niebisch and Bott, 2003). Its absence in the cryo-EM structure might be due to loss during size exclusion chromatography.

The structure of the *M. smegmatis* supercomplex showed a SodC-type Cu-containing superoxide dismutase (SOD) dimer, which is also composed of a lipobox motif attached to a lipoprotein segment within the supercomplex (Gong et al., 2018; Wiseman et al., 2018; Yanofsky et al., 2021). AscE of the *C. glutamicum* supercomplex is located at the equivalent position of the *M. smegmatis* SodC N-terminal anchor (Figures 2A and S5) but no SOD was found attached to the *C. glutamicum* supercomplex. The genome of *C. glutamicum* strain used in the current study harbors only an Mn-containing SodA (El Shafey et al., 2008). It is possible that *M. smegmatis* produces more superoxide than *C. glutamicum*, which would explain the presence of a SOD subunit in the former. A comparison of accessory subunits in *M. smegmatis* and *C. glutamicum* is shown in Figure S5.

Densities attributed to putative lipid molecules (Palsdottir and Hunte, 2004) were found at 61 positions within the supercomplex. Cardiolipin (CL), commonly found in membranes that are involved in maintaining an electrochemical proton gradient (Kagan et al., 2014; Paradies et al., 2014), was identified at 14 positions. Four CL molecules are found at the interface of CIII and CIV in each half of the $CIII_2CIV_2$ supercomplex, consistent with a role in supporting supramolecular interactions in respiratory supercomplexes (Pfeiffer et al., 2003). A CL is also found at the monomer-monomer interface of the $CIII_2$ dimer and one CL is bound to CtaD facing AscA and QcrB, further suggesting a role in higher-order assembly of complexes. A final CL is found in a cavity defined by subunits CtaE and CtaF of CIV that are suggested to be used for O_2 diffusion to the catalytic site (Hofacker and Schulten, 1998; Wikström et al., 2018) (see below). All CLs are oriented with their negatively charged head groups toward the *n* side of the membrane (see Kagan et al., 2014). Unidentifiable lipids were modeled as hydrocarbon chains (Figure S6).

Overall structure of complex III_2

The FeS-containing ectodomain on the periplasmic side of QcrA is anchored by three transmembrane α-helices (TMH 1-3), one of which (TMH 1) is swapped between CIII monomers in the dimer and occupies the same position where the single transmembrane α-helix of the Rieske iron-sulfur protein is found in the canonical CIII (Figure 2B, colored in dark blue). The two additional transmembrane α-helices (TMH 2 and 3) from QcrA are formed by an ~80 residue N-terminal extension, not found in canonical CIII. TMH2 occupies the position where the transmembrane α-helix of subunit cyt. c_1 is found in canonical CIII, which in the *C. glutamicum* structure is shifted toward the middle of the supercomplex (see also Wiseman et al., 2018). The FeS ectodomain of the *C. glutamicum* CIII is fixed in the B position by the LpqE subunit on the periplasmic side of the protein, which was also noted in structures of the *M. smegmatis* supercomplex that had LpqE (Gong et al., 2018; Yanofsky et al., 2021). This tight interface between the QcrA ectodomain and cyt. *cc* would preclude movement of the ectodomain.

The QcrC subunit is composed of a di-heme cyt. *cc* (cyt. c_I and c_{II}, Figure 1, lower part) head domain and a transmembrane α-helix, which is displaced compared with that of the cyt. c_1 subunit in the canonical CIII (Figure 2B, colored in light blue). The C-terminal sequence of QcrC forms a single transmembrane α-helix that contacts QcrB. Cyt. c_I of the cyt. *cc* domain interacts with the QcrA ectodomain on the opposite side from the FeS center, while cyt. c_{II} is bound near the electron-accepting Cu_A site of CIV. This arrangement of cyt. c_I, cyt. c_{II}, and Cu_A provides an electronic connection between CIII and each CIV of the supercomplex.

Subunit QcrB (Figure 2B, colored in green) consists of eight transmembrane α-helices and harbors hemes b_L and b_H, which occupy the same positions as in the canonical (Hunte et al., 2000) and *M. smegmatis* (Gong et al., 2018; Wiseman et al., 2018) $CIII_2$. In addition, the Q_P and Q_N quinone-binding sites are defined in part by residues of QcrB. The C terminus of QcrB is extended by 137 residues, not present in the canonical CIII, on the cytoplasmic side of the supercomplex (Niebisch and Bott, 2001). About 20 of these residues form a loop that contacts the CIV subunit CtaD (Wiseman et al., 2018).

Quinone binding in complex III

The Q_P site is typically empty in X-ray crystal structures of canonical $CIII_2$ from a wide range of organisms, and was identified from

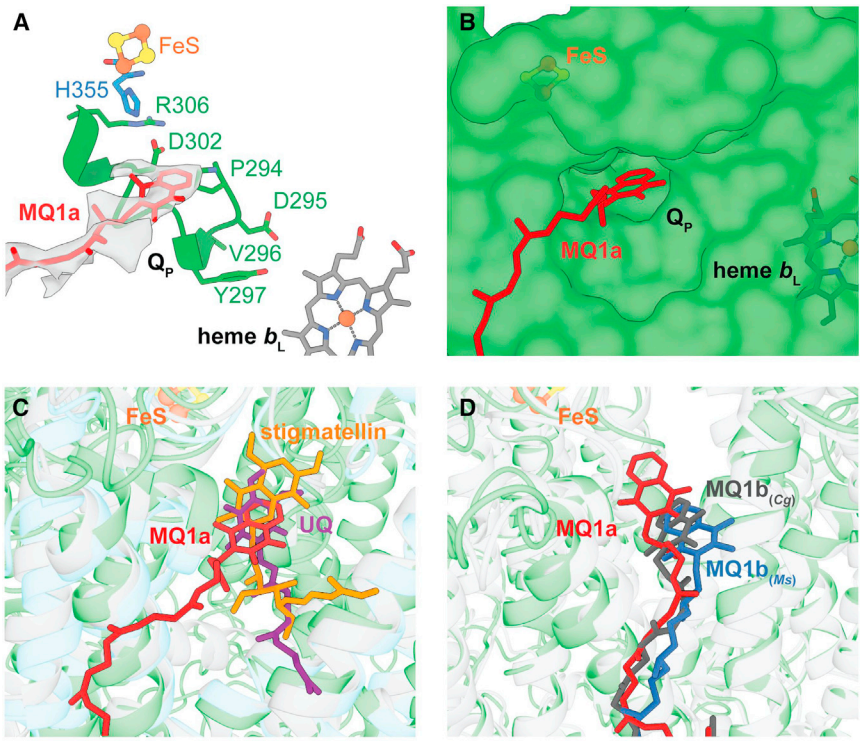

Figure 3. Q_P binding site in CIII

(A) Density modeled as an MQ in the QP site, MQ1a. Protonatable residues discussed in the text and the PDVY motif in the QcrB subunit are shown. Residue H355 is found in subunit QcrA.

(B) The Q_P site with bound MQ1a.

(C) Superposition of *C. glutamicum* CIII (green helices) with MQ bound in site MQ1a and UQ in *Ovis aries* (gray helices, PDB: 6Q9E), and stigmatellin in *Rhodobacter capsulatus* (blue helices, PDB: 1ZRT).

(D) MQ1a (colored in red) in *C. glutamicum* CIII overlaid with the MQ1b sites in *C. glutamicum* (colored in gray) and *M. smegmatis* (colored in blue) CIII, respectively.

the positions of the inhibitors stigmatellin and myxothiazol in inhibitor-bound structures of the complex (Sarewicz and Osyczka, 2015; Sarewicz et al., 2021). Recent cryo-EM studies revealed ubiquinone (UQ) bound at the Q_P site of the *C. albicans* $CIII_2$ (Di Trani et al., 2021) and in one monomer of $CIII_2$ from the mammalian CI-$CIII_2$ supercomplex (Letts et al., 2019). The map of $CIII_2CIV_2$ supercomplex reveals density for MQ adjacent to the FeS cluster in each CIII monomer, thereby defining the Q_P site in *C. glutamicum* (Figures 3A and 3B). This site overlaps with the UQ site identified in mammalian CIII (Letts et al., 2019) (Figure 3C). We designate the MQ molecule in this position as MQ1a. In structures of the *M. smegmatis* supercomplex density was seen at a distal position near the entrance to the Q_P cavity (Gong et al., 2018; Wiseman et al., 2018; Yanofsky et al., 2021), which we designated as MQ1b (Figure 3D).

The Q_P cavity in *C. glutamicum* CIII is larger than in the *M. smegmatis* enzyme. The density corresponding to MQ observed in the Q_P site of the *C. glutamicum* CIII is diffuse, spanning across a position equivalent to MQ1b. With the standard deviation of the cryo-EM map normalized to $\sigma = 1$, the density for the head group of MQ is visible at 3.4σ and the tail at 2.8σ, compared with the 3.0σ threshold where lipids are visible. This diffuse density could correspond to a single MQ bound only at MQ1a, or to averaging of two CIII populations in which one MQ bound in either MQ1a or MQ1b. In either case, observation of MQ at positions MQ1a or MQ1b in *C. glutamicum* and *M. smegmatis*, respectively, suggests that there are two possible binding modes in or just outside of the Q_P site, respectively (Figure 3D). Two QH_2 binding positions were suggested in a proposed mechanism for canonical $CIII_2$ in which QH_2 initially binds in a "stand-by" site and is then relocated into an oxidation site that is formed transiently after docking of the FeS domain in the B position (Mulkidjanian, 2005).

Furthermore, early EPR data indicated two Q-binding positions in the Q_P site of *R. capsulatus* cyt. bc_1 (Ding et al., 1992). Two possible MQ binding positions inside and just outside of the Q_P cavity is also reminiscent of the two Q-binding positions near the Q_B site in a crystal structure of a dark-adapted photosynthetic reaction center from *Rhodobacter sphaeroides* (Stowell et al., 1997).

Structural studies of the *M. smegmatis* $CIII_2CIV_2$ supercomplex (Gong et al., 2018; Wiseman et al., 2018; Yanofsky et al., 2021) identified density corresponding to MQ in an unexpected location, near the Tyr of the PDFY motif in CIII, which is equivalent to the canonical PEWY Q-binding motif (Kao and Hunte, 2014). This MQ is at the vertex of a triangle formed with heme b_L (~20 Å) and the FeS center (~20 Å) (Figure 4A). In the *C. glutamicum* structure, the corresponding position in the enzyme cannot accommodate MQ because it is occupied by Trp265 (Figure 4B). The positions of Trp265 in *C. glutamicum* and the equivalent Trp276 in *M. smegmatis* differ, presumably because the former accommodates a smaller Val instead of Phe in its Q-binding motif (PDVY in *C. glutamicum*) (Figures 4B and 4C). In *C. glutamicum* we observed MQ, which we designate MQ2 at a different location at the *p* side of the membrane, 14 Å from heme b_L and 30 to 35 Å from the Q_P site (Figure 4A). The density at MQ2 is stronger than at the MQ1 site, the head group is visible at 4.5σ and the tail at 3.5σ. The equivalent location in the *M. smegmatis* structures harbors a lipid tail density (Gong et al., 2018; Wiseman et al., 2018). Identification of a second Q-binding site on the *p* side of CIII in both *C. glutamicum* and *M. smegmatis* suggests a functional role, which is discussed below.

MQ is also found in the Q_N site (Figure S7 colored in pink), with the head group at the same position seen previously in the canonical (Hunte et al., 2000) and *M. smegmatis* (Gong et al., 2018; Wiseman et al., 2018) CIII.

The Q-cycle of complex III

The bifurcated electron transfer from QH_2 at the Q_P site is fundamental for the Q-cycle mechanism that conserves energy in CIII (Figure 1) (Osyczka et al., 2005). As outlined in the introduction section, in this process the first electron

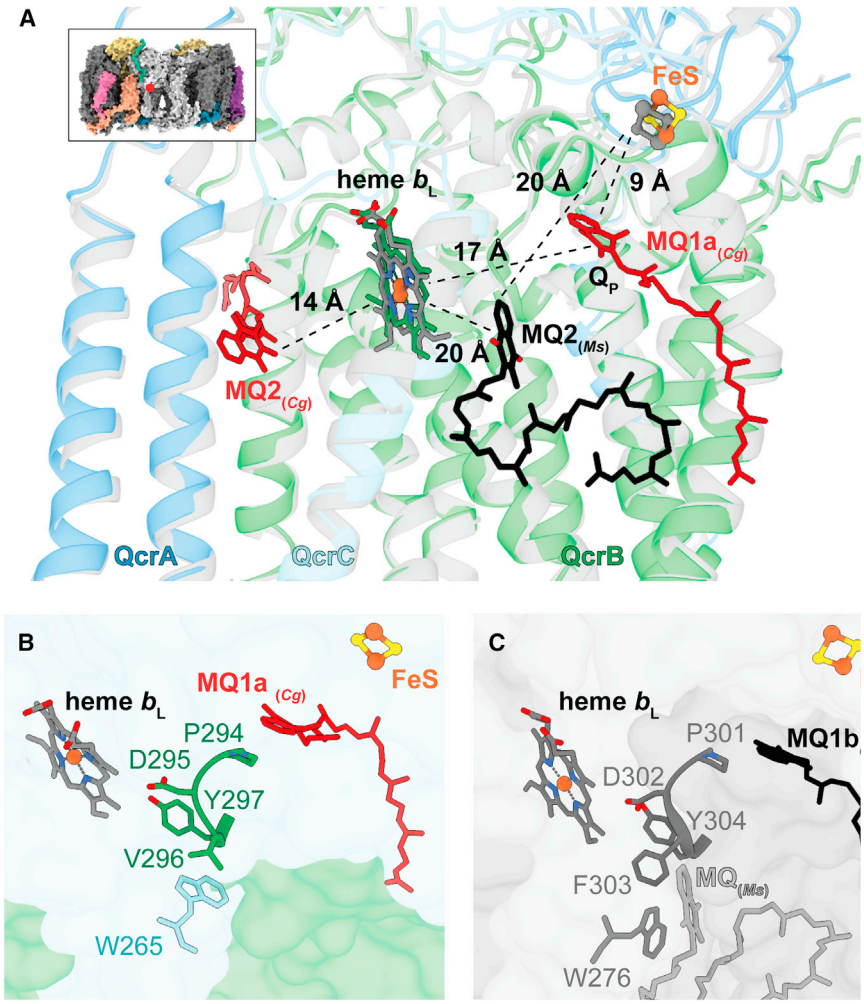

Figure 4. Q-binding sites on the periplasmic side of *C. glutamicum* and *M. smegmatis*

(A) Position of MQ1a in relation to the FeS cluster and heme b_L, as well as a second MQ in site MQ2. The position of MQ2 in *M. smegmatis* CIII (*Ms* in black) is overlaid on the structure of *C. glutamicum* CIII. In the inset the approximate position of this area in one CIII monomer of the supercomplex is marked with a red circle.

(B) Structure of a segment of *C. glutamicum* CIII where MQ2 is found in *M. smegmatis*. In *C. glutamicum*, binding of MQ in this location is obstructed by W265, which adopts a different position than in *M. smegmatis* due to the presence of a smaller V296 in the conserved Q-binding loop (PDVY). MQ1a is shown for reference.

(C) The *M. smegmatis* MQ2 binding site ($MQ_{(Ms)}$) and the conserved Q-binding loop (PDFY). MQ1b is shown for reference.

from QH_2 is transferred to FeS, while the second is transferred to heme b_L in a concerted mechanism:

$$QH_2\ FeS\ b_L \underset{k_{-1}}{\overset{k_1}{\rightleftarrows}} SQ^{\bullet-}\ FeS^-\ b_L \overset{k_2}{\rightarrow} Q\ FeS^-\ b_L^- \qquad \text{(Equation 1)}$$

In canonical CIII, rotation of the FeS domain from the electron-receiving B position to the electron-donating C position near cyt. c_1 is thought to be part of the mechanism that allows bifurcated electron transfer (Berry et al., 2013; Mulkidjanian, 2005; Sarewicz and Osyczka, 2015; Sarewicz et al., 2021).

Oxidation of QH_2 at the Q_P site has been studied primarily with the canonical CIII (Berry and Huang, 2003; Hunte et al., 2003; Mulkidjanian, 2005; Sarewicz et al., 2021). Upon QH_2 binding, the FeS domain moves to the B position, and QH_2 forms a hydrogen bond with the FeS ligand His181 (*S. cerevisiae* numbering), which also receives a proton from QH_2 upon electron transfer to FeS (Brandt and Okun, 1997; Crofts et al., 1999; Iwaki et al., 2005; Rich, 2004). The second electron is transferred to heme b_L, along with proton transfer, presumably to Glu272, which is part of the Q-binding PEWY motif in *S. cerevisiae* (Crofts et al., 1999; Hunte et al., 2003; Mulkidjanian, 2005). The proton-ated Glu272 is suggested to rotate toward the heme b_L propionate, which transiently binds the proton (Crofts et al., 1999; Hunte et al., 2003) before it is released to the *p* side aqueous phase. After transfer of the second electron to heme b_L, the FeS domain moves to the C position, which allows electron transfer to cyt. c_1 and release of the proton from His181 to the aqueous phase on the *p* side.

As in the *M. smegmatis* CIII, in *C. glutamicum* the FeS domain is locked in the B position (Gong et al., 2018; Wiseman et al., 2018; Yanofsky et al., 2021). Therefore, a mechanism other than movement of the FeS domain must exist to explain the proton-coupled electron transfer reactions linked to MQH_2 oxidation. In one of the structures of the *M. smegmatis* supercomplex, the cyt. *cc* domain was found to adopt two conformations, one in which CIII and CIV are electronically connected, and one in which this connection is disrupted. This dynamic of the cyt. *cc* domain was suggested to be involved in Q-cycle electron gating in analogy with the FeS domain movement (Wiseman et al., 2018). A more recent structure of the *M. smegmatis* $CIII_2CIV_2$ supercomplex showed that the dynamics of the cyt. *cc* domain is only possible in the absence of subunit LpqE (Yanofsky et al., 2021), which was missing in one of the earlier structures (Wiseman et al., 2018). Nevertheless, even though dynamic cyt. *cc* and FeS domains have been observed, this movement is not required for electron bifurcation (Jünemann et al., 1998).

In *C. glutamicum* both the FeS and cyt. *cc* domains are fixed. Similar to the canonical CIII (see above), we hypothesize that in the *C. glutamicum* enzyme an electron and a proton are transferred from MQH_2 in the Q_P site to FeS and its His355 ligand (see Figure 3A), respectively (Figure 5, e^-_1 and H^+_1, top left). The equivalent of *S. cerevisiae* Glu272 in *C. glutamicum* is Asp295 (Figure 3A) of the PDVY motif, which is located near the heme b_L propionates, but the Asp side chain is too short

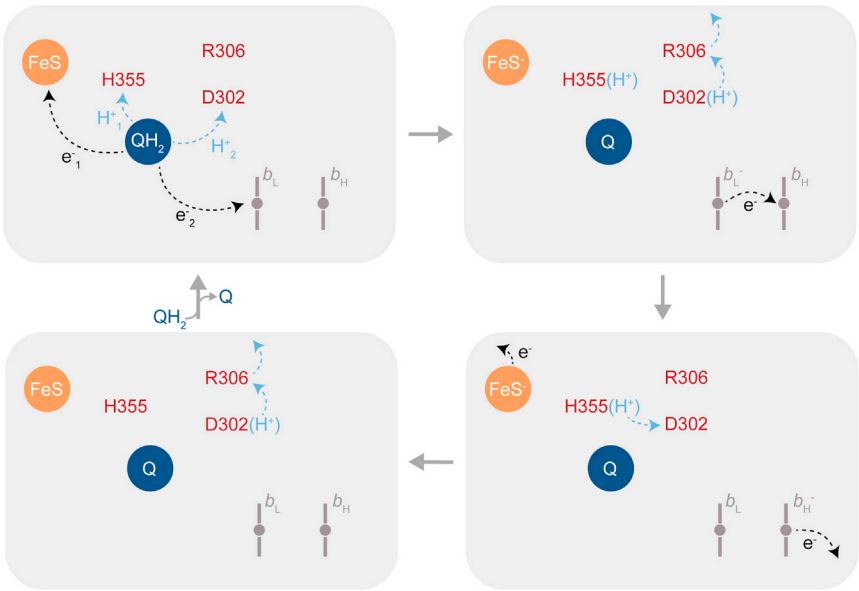

Figure 5. The Q-cycle electron bifurcation in *C. glutamicum* CIII

The model is based on earlier studies with canonical CIII (Berry and Huang, 2003; Hunte et al., 2003; Mulkidjanian, 2005; Sarewicz et al., 2021), but adapted to residues identified in the *C. glutamicum* CIII. The first electron and proton from MQH_2 are transferred to FeS and His355, respectively. The second electron and proton are transferred to heme b_L and Asp302, respectively. After this charge separation electron transfer from FeS^- (to heme *c*, not shown) is not possible because His355 cannot be deprotonated until the proton is released from Asp302. This sequence of events ensures that the second electron is transferred along the B branch before the first electron is transferred along the C branch.

to reach MQH_2 in the Q_P site to accept a proton. Instead, Asp302 (Figure 3A), located ~5 Å from MQH_2 in the Q_P site could receive a proton upon concerted transfer of the second electron from $SQ^{\bullet-}$ to heme b_L (Figure 5, e^-_2 and H^+_2, top left). Residue Asp302 is not conserved, but in other Actinobacteria it is replaced by a Glu residue, which could also serve as a proton acceptor. Arg306, which is highly conserved, is ~3 Å from Asp302 (Figure 3A), which points to a possible route for proton release to the *p* side aqueous solution (Figure 5, top right). Even though the side chain pK_a of Arg is likely to be high, Arg and Lys residues have been found to be part of proton-transfer pathways, e.g., in bacteriorhodopsin and CIV (K pathway) (Brzezinski and Ädelroth, 1998; Lanyi, 2004). Interestingly, Asp302 is ~3 Å from His355, suggesting that this residue is also on a proton-transfer pathway from His355. This architecture offers a plausible mechanism for Q-cycle electron branching in *C. glutamicum* that is guided by local proton-transfer reactions in the protein matrix. We suggest that after the initial oxidation of MQH_2 (Figure 5, top left), the electron is stabilized by the His355 proton. Thus, electron transfer from FeS^- to heme c_I is not possible because His355 cannot be deprotonated until H^+_2 is released from Asp302. If electron transfer from heme b_L to heme b_H occurs as fast as proton transfer from Asp302 to the *p* side (Figure 5, top right), charge separation along the B branch is accomplished while FeS remains in the reduced state, FeS^-. The FeS ligand His355 can become deprotonated only after Asp302 loses its proton, which allows electron transfer from FeS^- to heme c_I, along the C branch (Figure 5, bottom right). In the final step of the reaction, the second proton from Asp302 is released via Arg306 (Figure 5, bottom left). This model is supported by the observation that the $FeS^- \rightarrow$ heme c_I electron transfer is the slowest of the measured electron transfer reactions in the *C. glutamicum* supercomplex (Graf et al., 2016).

A second MQ is found at the *p* side of the supercomplex, 14 Å from heme b_L (MQ2 in Figure 4A). The position of MQ2 is different from that observed in the *M. smegmatis* enzyme (Gong et al., 2018; Wiseman et al., 2018) (Figure 4A). The role of this MQ is unknown, but we speculate that it may be functionally relevant because a secondary site was also observed in the *M. smegmatis* supercomplex. Electron transfer via the MQ2 site could provide an alternative electron path that bypasses heme b_H, thereby decoupling electron transfer through the CIII portion of the supercomplex from generation of a PMF and preventing energy conservation. This pathway would maintain an electron flux through the respiratory chain, for example at low O_2 concentrations (Zelle et al., 2021) or at an increased MQ-reduction rate. An electron bypass route does not require a fixed location of the secondary MQ2-binding site, which would explain why different locations were identified in the *C. glutamicum* and *M. smegmatis* CIII (Figure 4A).

Complex IV

The core subunits of *C. glutamicum* CIV, CtaC and CtaD, are homologous to conserved subunits (SU) II and I, respectively, of canonical CIV (Figure 2C, light pink and red, respectively). These subunits harbor all redox-active metal cofactors of CIV. Subunit CtaC is composed of two transmembrane α-helices and a head domain, which binds the primary electron acceptor, Cu_A. Subunit CtaD is composed of 12 transmembrane α-helices, which bind heme *a* and the catalytic site, which includes heme a_3 and Cu_B. The relative positions of the redox-active cofactors within CtaC and CtaD are the same in *C. glutamicum* as in CIV from other organisms (Figure 6). In canonical CIV, the seven transmembrane α-helices of SU III form a V-shaped O_2 channel (Hofacker and Schulten, 1998; Wikström et al., 2018) that harbors three tightly bound lipid molecules (Qin et al., 2007). As with the *M. smegmatis* supercomplex (Gong et al., 2018; Wiseman et al., 2018; Yanofsky et al., 2021), SU III from canonical CIV is replaced in the *C. glutamicum* enzyme by two proteins, CtaE and CtaF (Figure 2C, orange and yellow, respectively), harboring a single CL molecule (Figure S6). The division of SU III into two parts resembles the supercomplex structure of alternative complex III (ACIII) and CIV in *Flavobacterium johnsoniae* where the

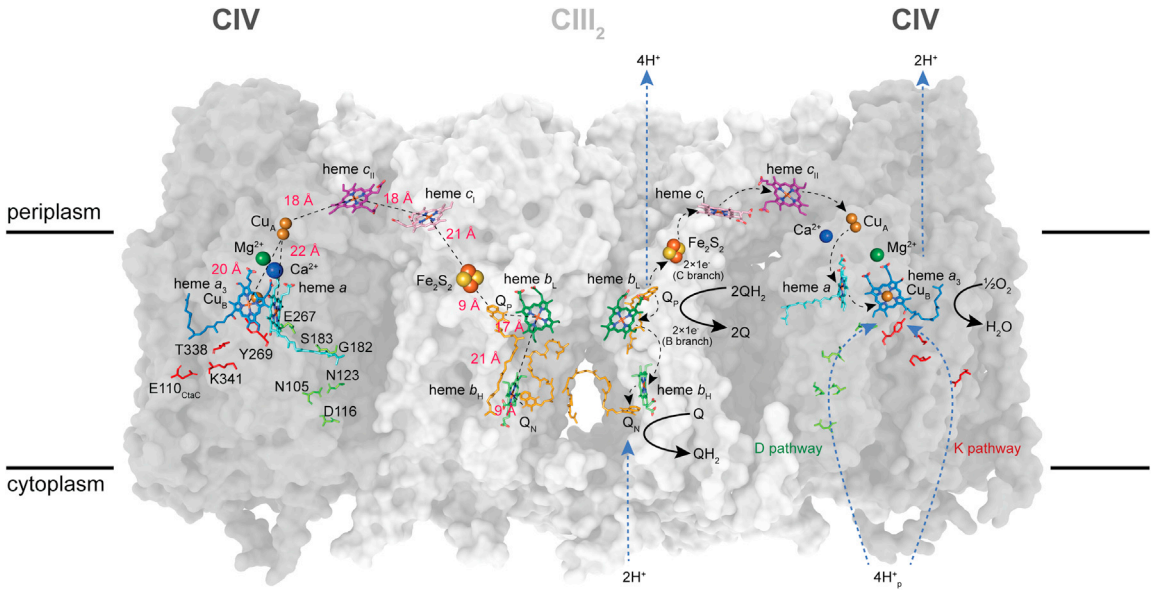

Figure 6. The *C. glutamicum* supercomplex

The right- and left-hand side halves of the supercomplex show the reactions catalyzed by CIII and CIV, and distances between the cofactors, respectively. Residues of the D and K pathways in CIV are labeled in the left-hand side.

equivalent of SU III has lost the first two transmembrane α-helices (equivalent of CtaF) (Sun et al., 2018).

Previous structures of mammalian, *S. cerevisiae*, and bacterial CIV revealed a Mg^{2+} ion 12 Å from Cu_B and 13 Å from the heme a_3 iron (Hartley et al., 2019; Hosler et al., 1995; Ostermeier et al., 1997; Tsukihara et al., 1996). In addition, a Na^+ or Ca^{2+} ion was found to be bound in mitochondrial and bacterial CIV, respectively, at a site on the *p* side of CIV (Hartley et al., 2019; Ostermeier et al., 1997; Tsukihara et al., 1996). In the present structure we found densities at both positions, which we modeled as Mg^{2+} and Ca^{2+}, respectively (Figure 6, green and blue spheres, respectively).

The supercomplex structure reveals both the K and D proton pathways in CIV. In analogy with previously studied CIVs, the K proton pathway, used for proton transfer to the catalytic site upon reduction of heme a_3 and Cu_B, starts near the *n* side surface at Glu110 (CtaC), and is lined by several CtaD residues, including the conserved central Lys341 as well as Tyr269 at the catalytic site (Fetter et al., 1995; Hosler et al., 1996; Konstantinov et al., 1997; Ädelroth et al., 1998). In analogy with previously studied bacterial CIVs, the D proton pathway is defined by the highly conserved Asp116 in the inner part of a cavity in CtaD and several polar residues that span the distance to the highly conserved Glu267 of the XGHPEVY motif (Figures 6 and 7). X-ray crystal structures of CIV from other organisms also revealed about 10 water molecules that span the distance between Asp116 and Glu267 (Iwata et al., 1995; Qin et al., 2006; Svensson-Ek et al., 2002; Tsukihara et al., 1996), but these water molecules could not be resolved in the current cryo-EM map. The D pathway is used for proton transfer to the catalytic site as well as for proton pumping to the *p* side of the membrane after binding of O_2 to heme a_3 (Fetter et al., 1995; Hosler et al., 1996; Konstantinov et al., 1997; Ädelroth et al., 1997).

Cytoplasmic side sub-structure

At the cytoplasmic side of the *C. glutamicum* supercomplex, multiple subunits interact to create an intricate sub-structure, which includes secondary structure elements from CtaD, the C terminus of AscA, a CtaF loop, AscC, and the N and C termini of AscD (Figure 7). The equivalent sub-structure of the *M. smegmatis* supercomplex is composed of fewer components, primarily subunits MSMEG_4692 (CtaI) and MSMEG_4693 (CtaJ) (Gong et al., 2018; Wiseman et al., 2018) that are not present in the *C. glutamicum* supercomplex. Interestingly, as seen in the *M. smegmatis* supercomplex, the 20-residue QcrB loop (see above) covers the proton-uptake cavity around Asp116 (Figure 7), which in the canonical CIV is exposed to the *n* side aqueous solution. Conservation of this feature in both the *M. smegmatis* and *C. glutamicum* supercomplexes (Figure S5E) suggests a functional role. Mutation of the equivalent of Asp116 or residues in its vicinity in other CIVs result in drastic changes in the proton-uptake rate or uncoupling of proton pumping from O_2 reduction (Brzezinski and Johansson, 2010; Johansson et al., 2013; Smirnova et al., 1999). Furthermore, mutation of a Glu residue in a C-terminal flexible loop in *R. sphaeroides* CIV, 10 Å "below" the equivalent of Asp116, near the QcrB extension loop in the *C. glutamicum* structure, resulted in a decrease in the proton-pumping stoichiometry by a factor of two (Berg et al., 2020). Collectively, these data show that the area around the D pathway opening is critical for determining proton-uptake kinetics, presumably by tuning the electrostatic potential, thereby providing a proton-collecting antenna (Marantz et al., 1998). In addition, in *C. glutamicum* a chain of Asp, Glu, and His residues at the C terminus of QcrB provide an alternative proton path from the *n* side surface to Asp116 (Figure 7).

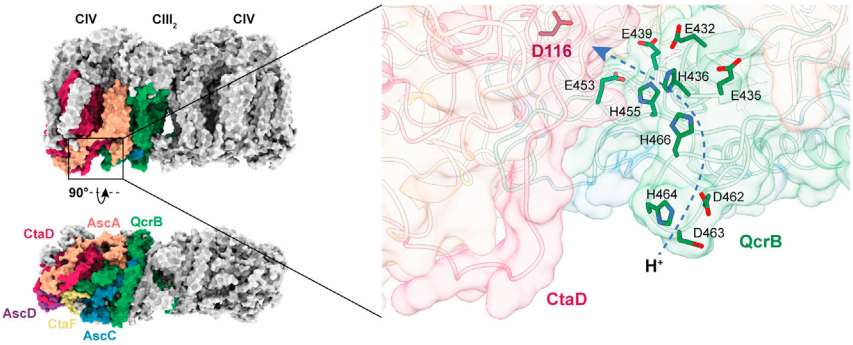

Figure 7. Cytoplasmic side sub-structure

The entry point of the D pathway in complex IV. Subunits that contribute residues that define the entry point of the D pathway of CIV are shown in color. A complex III QcrB loop (green) forms a "lid" over the D pathway entry point cavity. This "lid" harbors a number of protonatable residues that define a proton pathway leading from the cytoplasmic side to the D pathway entry point defined by Asp116.

Electron transfer from QH_2 to O_2

Complexes III and IV are electronically connected by the cyt. *cc* domain of the QcrC subunit of CIII. In the *C. glutamicum* structure, the distance between FeS and cyt. c_I is 21 Å (Figure 6). Assuming a $\Delta G^0 \cong +60$ meV (Kao et al., 2016) and a reorganization energy of 0.7 eV yields a time constant for electron transfer from FeS to cyt. c_I of ~10 ms (Gray and Winkler, 2005), which is consistent with the measured value of ~6.5 ms for oxidation of the *C. glutamicum* CIII (Graf et al., 2016). The Fe-Fe distances between hemes c_I and c_{II}, and between heme c_{II} and Cu_A are both ~18 Å (Figure 1) yielding calculated time constants of ~1 ms for each electron transfer. Kinetic data showed biphasic oxidation of cyt. *cc* suggesting a time constant for electron transfer to Cu_A in the range 100 μs to 2 ms (Graf et al., 2016), which is consistent with the estimated value.

Conclusions

This study reveals the structure of the respiratory $CIII_2CIV_2$ supercomplex from *C. glutamicum*. The structure shows MQ bound inside the Q_P site cavity and offers insights into how Actinobacteria enable energy-conserving Q-cycle electron bifurcation without the mobile FeS domain found in canonical CIII. The structure shows a D proton pathway at the opening of CIV where residues from the neighboring QcrB subunit provide a proton-entry route from the *n* side. These findings illustrate the wide variety of structures that allow realization of respiratory pathways in aerobic organisms with particular insight into respiration in Actinobacteria.

STAR★METHODS

Detailed methods are provided in the online version of this paper and include the following:

- KEY RESOURCES TABLE
- RESOURCE AVAILABILITY
  - Lead contact
  - Materials availability
  - Data and code availability
- EXPERIMENTAL MODEL AND SUBJECT DETAILS
- METHOD DETAILS
  - Membrane preparation
  - Isolation of supercomplexes
  - Spectral analysis
  - Preparation of menaquinol
  - Activity assays
  - Gel electrophoresis
  - Grid preparation and cryo-electron microscopy
  - Image analysis
  - Model building and refinement
- QUANTIFICATION AND STATISTICAL ANALYSIS

SUPPLEMENTAL INFORMATION

Supplemental information can be found online at https://doi.org/10.1016/j.str.2021.11.008.

ACKNOWLEDGMENTS

We thank Mikael Oliveberg for valuable discussions. This work was supported by the Knut and Wallenberg Foundation (M.H., P.B.), the Swedish Research Council (M.H., P.B.), and Canadian Institutes of Health Research grant PJT162186 (J.L.R.). J.L.R. was supported by the Canada Research Chairs program. Cryo-EM data was collected at the Swedish National Cryo-EM Facility funded by the Knut and Alice Wallenberg, Family Erling Persson and Kempe Foundations, SciLifeLab, Stockholm University, and Umeå University. Mass spectrometry was done at the Mass Spectrometry-based Proteomics Facility at Uppsala University.

AUTHOR CONTRIBUTIONS

J.L.R., M.H., and P.B. designed the research; A.M., T.K., S.K., D.J.Y., and D.S. performed research; A.M., T.K., M.B., D.S., J.L.R., M.H., and P.B. analyzed and interpreted the data; D.S., J.L.R., M.H., and P.B. supervised the research; and A.M., T.K., M.B., D.S., J.L.R., M.H., and P.B. wrote the paper.

DECLARATION OF INTERESTS

The authors declare no competing interests.

Received: May 28, 2021
Revised: September 29, 2021
Accepted: November 18, 2021
Published: December 14, 2021

REFERENCES

Ädelroth, P., Svensson Ek, M., Mitchell, D.M., Gennis, R.B., and Brzezinski, P. (1997). Glutamate 286 in cytochrome aa_3 from *Rhodobacter sphaeroides* is involved in proton uptake during the reaction of the fully-reduced enzyme with dioxygen. Biochemistry *36*, 13824–13829.

Ädelroth, P., Gennis, R.B., and Brzezinski, P. (1998). Role of the pathway through K(I-362) in proton transfer in cytochrome *c* oxidase from *R. sphaeroides*. Biochemistry *37*, 2470–2476.

Afonine, P.V., Poon, B.K., Read, R.J., Sobolev, O.V., Terwilliger, T.C., Urzhumtsev, A., and Adams, P.D. (2018). Real-space refinement in PHENIX for cryo-EM and crystallography. Acta Crystallogr. D Struct. Biol. *74*, 531–544.

Altschul, S.F., Gish, W., Miller, W., Myers, E.W., and Lipman, D.J. (1990). Basic local alignment search tool. J. Mol. Biol. *215*, 403–410.

Berg, J., Liu, J., Svahn, E., Ferguson-Miller, S., and Brzezinski, P. (2020). Structural changes at the surface of cytochrome *c* oxidase alter the proton-pumping stoichiometry. Biochim. Biophys. Acta *1861*, 148116.

Berry, E.A., and Huang, L.S. (2003). Observations concerning the quinol oxidation site of the cytochrome bc_1 complex. FEBS Lett. *555*, 13–20.

Berry, E.A., De Bari, H., and Huang, L.S. (2013). Unanswered questions about the structure of cytochrome bc_1 complexes. Biochim. Biophys. Acta *1827*, 1258–1277.

Bott, M., and Niebisch, A. (2003). The respiratory chain of *Corynebacterium glutamicum*. J. Biotechn *104*, 129–153.

Brandt, U., and Okun, J.G. (1997). Role of deprotonation events in ubihydroquinone:cytochrome *c* oxidoreductase from bovine heart and yeast mitochondria. Biochemistry *36*, 11234–11240.

Brzezinski, P., and Ädelroth, P. (1998). Pathways of proton transfer in cytochrome *c* oxidase. J. Bioenerg. Biomembr. *30*, 99–107.

Brzezinski, P., and Gennis, R.B. (2008). Cytochrome c oxidase: exciting progress and remaining mysteries. J. Bioenerg. Biomembr. *40*, 521–531.

Brzezinski, P., and Johansson, A.L. (2010). Variable proton-pumping stoichiometry in structural variants of cytochrome *c* oxidase. Biochim. Biophys. Acta *1797*, 710–723.

Brzezinski, P., Moe, A., and Ädelroth, P. (2021). Structure and mechanism of respiratory III–IV supercomplexes in bioenergetic membranes. Chem. Rev. *121*, 9644–9673.

Cramer, W.A., Hasan, S.S., and Yamashita, E. (2011). The Q cycle of cytochrome *bc* complexes: a structure perspective. Biochim. Biophys. Acta *1807*, 788–802.

Crofts, A.R. (2004). The cytochrome bc_1 complex: function in the context of structure. Annu. Rev. Physiol. *66*, 689–733.

Crofts, A.R. (2021). The modified Q-cycle: a look back at its development and forward to a functional model. Biochim. Biophys. Acta Bioenerg. *1862*, 148417.

Crofts, A.R., Hong, S.J., Ugulava, N., Barquera, B., Gennis, R., Guergova-Kuras, M., and Berry, E.A. (1999). Pathways for proton release during ubihydroquinone oxidation by the bc(1) complex. Proc. Natl. Acad. Sci. U S A *96*, 10021–10026.

Davoudi, C.-F., Ramp, P., Baumgart, M., and Bott, M. (2019). Identification of Surf1 as an assembly factor of the cytochrome bc1-aa3 supercomplex of Actinobacteria. Biochim. Biophys. Acta Bioenerg. *1860*, 148033.

Ding, H., Robertson, D.E., Dutton, P.L., and Daldal, F. (1992). Cytochrome bc1 complex [2Fe-2S] cluster and its interaction with ubiquinone and ubihydroquinone at the Qo site: a double-occupancy Qo site model. Biochemistry *31*, 3144–3158.

Eggeling, L., and Bott, M. (2015). A giant market and a powerful metabolism: l-lysine provided by Corynebacterium glutamicum. Appl. Microbiol. Biotechnol. *99*, 3387–3394.

El Shafey, H.M., Ghanem, S., Merkamm, M., and Guyonvarch, A. (2008). Corynebacterium glutamicum superoxide dismutase is a manganese-strict non-cambialistic enzyme in vitro. Microbiol. Res. *163*, 80–86.

Emsley, P., Lohkamp, B., Scott, W.G., and Cowtan, K. (2010). Features and development of Coot. Acta Crystallogr. D Biol. Crystallogr. *66*, 486–501.

Fetter, J.R., Qian, J., Shapleigh, J., Thomas, J.W., García-Horsman, A., Schmidt, E., Hosler, J., Babcock, G.T., Gennis, R.B., and Ferguson-Miller, S. (1995). Possible proton relay pathways in cytochrome *c* oxidase. Proc. Natl. Acad. Sci. U S A *92*, 1604–1608.

Gong, H., Li, J., Xu, A., Tang, Y., Ji, W., Gao, R., Wang, S., Yu, L., Tian, C., Li, J., et al. (2018). An electron transfer path connects subunits of a mycobacterial respiratory supercomplex. Science *362*, 1–11.

Graf, S., Fedotovskaya, O., Kao, W.C., Hunte, C., Ädelroth, P., Bott, M., Von Ballmoos, C., and Brzezinski, P. (2016). Rapid electron transfer within the III-IV supercomplex in *Corynebacterium glutamicum*. Sci. Rep. *6*, 34098.

Gray, H.B., and Winkler, J.R. (2005). Long-range electron transfer. Proc. Natl. Acad. Sci. U S A *102*, 3534–3539.

Hartley, A.M., Lukoyanova, N., Zhang, Y., Cabrera-Orefice, A., Arnold, S., Meunier, B., Pinotsis, N., and Maréchal, A. (2019). Structure of yeast cytochrome *c* oxidase in a supercomplex with cytochrome bc_1. Nat. Struct. Mol. Biol. *26*, 78–83.

Hashimoto, S.I. (2017). Discovery and history of amino acid fermentation. Adv. Biochem. Eng. Biotechnol. *159*, 15–34.

Hemp, J., and Gennis, R.B. (2008). Diversity of the heme-copper superfamily in archaea: insights from genomics and structural modeling. Results Probl. Cell Differ. *45*, 1–31.

Hofacker, I., and Schulten, K. (1998). Oxygen and proton pathways in cytochrome *c* oxidase. Proteins *30*, 100–107.

Hosler, J.P., Espe, M.P., Zhen, Y., Babcock, G.T., and Ferguson-Miller, S. (1995). Analysis of site-directed mutants locates a non-redox-active metal near the active site of cytochrome *c* oxidase of *Rhodobacter sphaeroides*. Biochemistry *34*, 7586–7592.

Hosler, J.P., Shapleigh, J.P., Mitchell, D.M., Kim, Y., Pressler, M.A., Georgiou, C., Babcock, G.T., Alben, J.O., Ferguson-Miller, S., and Gennis, R.B. (1996). Polar residues in helix VIII of subunit I of cytochrome *c* oxidase influence the activity and the structure of the active site. Biochemistry *35*, 10776–10783.

Hosler, J.P., Ferguson-Miller, S., and Mills, D.A. (2006). Energy transduction: proton transfer through the respiratory complexes. Annu. Rev. Biochem. *75*, 165–187.

Hunte, C., Koepke, J., Lange, C., Roßmanith, T., and Michel, H. (2000). Structure at 2.3 Å resolution of the cytochrome bc1 complex from the yeast *Saccharomyces cerevisiae* co-crystallized with an antibody Fv fragment. Structure *8*, 669–684.

Hunte, C., Palsdottir, H., and Trumpower, B.L. (2003). Protonmotive pathways and mechanisms in the cytochrome bc_1 complex. FEBS Lett. *545*, 39–46.

Iwaki, M., Yakovlev, G., Hirst, J., Osyczka, A., Dutton, P.L., Marshall, D., and Rich, P.R. (2005). Direct observation of redox-linked histidine protonation changes in the iron–sulfur protein of the cytochrome bc_1 complex by ATR-FTIR spectroscopy. Biochemistry *44*, 4230–4237.

Iwata, S., Ostermeier, C., Ludwig, B., and Michel, H. (1995). Structure at 2.8 Å resolution of cytochrome *c* oxidase from *Paracoccus denitrificans*. Nature *376*, 660–669.

Johansson, A.L., Högbom, M., Carlsson, J., Gennis, R.B., and Brzezinski, P. (2013). Role of aspartate 132 at the orifice of a proton pathway in cytochrome *c* oxidase. Proc. Natl. Acad. Sci. U S A *110*, 8912–8917.

Jünemann, S., Heathcote, P., and Rich, P.R. (1998). On the mechanism of quinol oxidation in the bc_1 complex. J. Biol. Chem. *273*, 21603–21607.

Kagan, V.E., Chu, C.T., Tyurina, Y.Y., Cheikhi, A., and Bayir, H. (2014). Cardiolipin asymmetry, oxidation and signaling. Chem. Phys. Lipids *179*, 64–69.

Kao, W.C., and Hunte, C. (2014). The molecular evolution of the Q_o Motif. Genome Biol. Evol. *6*, 1894–1910.

Kao, W.C., Kleinschroth, T., Nitschke, W., Baymann, F., Neehaul, Y., Hellwig, P., Richers, S., Vonck, J., Bott, M., and Hunte, C. (2016). The obligate respiratory supercomplex from Actinobacteria. Biochim. Biophys. Acta *1857*, 1705–1714.

Kinoshita, S., Udaka, S., and Shimono, M. (1957). Studies on the amino acid fermentation Part I. Production of L-glutamic acid by various microorganisms. J. Gen. Appl. Microbiol. *3*, 193–205.

Konstantinov, A.A., Siletsky, S., Mitchell, D., Kaulen, A., and Gennis, R.B. (1997). The roles of the two proton input channels in cytochrome *c* oxidase from Rhodobacter sphaeroides probed by the effects of site-directed mutations on time-resolved electrogenic intraprotein proton transfer. Proc. Natl. Acad. Sci. U S A *94*, 9085–9090.

Lanyi, J.K. (2004). Bacteriorhodopsin. Annu. Rev. Physiol. *66*, 665–688.

Lee, H.M., Das, T.K., Rousseau, D.L., Mills, D., Ferguson-Miller, S., and Gennis, R.B. (2000). Mutations in the putative H-channel in the cytochrome *c* oxidase from *Rhodobacter sphaeroides* show that this channel is not important for proton conduction but reveal modulation of the properties of heme *a*. Biochemistry *39*, 2989–2996.

Lee, H.J., Reimann, J., Huang, Y., and Ädelroth, P. (2012). Functional proton transfer pathways in the heme-copper oxidase superfamily. Biochim. Biophys. Acta *1817*, 537–544.

Letts, J.A., Fiedorczuk, K., Degliesposti, G., Skehel, M., and Sazanov, L.A. (2019). Structures of rspiratory supercomplex I+III$_2$ reveal functional and conformational crosstalk. Mol. Cell *75*, 1131–1146.e1136.

Liebschner, D., Afonine, P.V., Baker, M.L., Bunkoczi, G., Chen, V.B., Croll, T.I., Hintze, B., Hung, L.W., Jain, S., McCoy, A.J., et al. (2019). Macromolecular structure determination using X-rays, neutrons and electrons: recent developments in Phenix. Acta Crystallogr. D Struct. Biol. *75*, 861–877.

Marantz, Y., Nachliel, E., Aagaard, A., Brzezinski, P., and Gutman, M. (1998). The proton collecting function of the inner surface of cytochrome c oxidase from Rhodobacter sphaeroides. Proc. Natl. Acad. Sci. U S A *95*, 8590–8595.

Megehee, J.A., Hosler, J.P., and Lundrigan, M.D. (2006). Evidence for a cytochrome *bcc-aa*$_3$ interaction in the respiratory chain of *Mycobacterium smegmatis*. Microbiology *152*, 823–829.

Mitchell, P. (1976). Possible molecular mechanisms of the protonmotive function of cytochrome systems. J. Theor. Biol. *62*, 327–367.

Morosov, X., Davoudi, C.-F., Baumgart, M., Brocker, M., and Bott, M. (2018). The copper-deprivation stimulon of Corynebacterium glutamicum comprises proteins for biogenesis of the actinobacterial cytochrome bc1–aa3 supercomplex. J. Biol. Chem. *293*, 15628–15640.

Mulkidjanian, A.Y. (2005). Ubiquinol oxidation in the cytochrome *bc*$_1$ complex: reaction mechanism and prevention of short-circuiting. Biochim. Biophys. Acta *1709*, 5–34.

Niebisch, A., and Bott, M. (2001). Molecular analysis of the cytochrome *bc*$_1$-*aa*$_3$ branch of the *Corynebacterium glutamicum* respiratory chain containing an unusual diheme cytochrome *c*$_1$. Arch. Microbiol. *175*, 282–294.

Niebisch, A., and Bott, M. (2003). Purification of a cytochrome *bc*$_1$-*aa*$_3$ supercomplex with quinol oxidase activity from *Corynebacterium glutamicum*: identification of a fourth subunit of cytochrome *aa*$_3$ oxidase and mutational analysis of diheme cytochrome *c*$_1$. J. Biol. Chem. *278*, 4339–4346.

Ostermeier, C., Harrenga, A., Ermler, U., and Michel, H. (1997). Structure at 2.7 Å resolution of the *Paracoccus denitrificans* two-subunit cytochrome *c* oxidase complexed with an antibody F$_V$ fragment. Proc. Natl. Acad. Sci. U S A *94*, 10547–10553.

Osyczka, A., Moser, C.C., and Dutton, P.L. (2005). Fixing the Q cycle. Trends Biochem. Sci. *30*, 176–182.

Palsdottir, H., and Hunte, C. (2004). Lipids in membrane protein structures. Biochim. Biophys. Acta Biomembr. *1666*, 2–18.

Paradies, G., Paradies, V., De Benedictis, V., Ruggiero, F.M., and Petrosillo, G. (2014). Functional role of cardiolipin in mitochondrial bioenergetics. Biochim. Biophys. Acta *1837*, 408–417.

Pereira, M.M., Santana, M., and Teixeira, M. (2001). A novel scenario for the evolution of haem-copper oxygen reductases. Biochim. Biophys. Acta *1505*, 185–208.

Pettersen, E.F., Goddard, T.D., Huang, C.C., Couch, G.S., Greenblatt, D.M., Meng, E.C., and Ferrin, T.E. (2004). UCSF Chimera - a visualization system for exploratory research and analysis. J. Comput. Chem. *25*, 1605–1612.

Pettersen, E.F., Goddard, T.D., Huang, C.C., Meng, E.C., Couch, G.S., Croll, T.I., Morris, J.H., and Ferrin, T.E. (2021). UCSF ChimeraX: structure visualization for researchers, educators, and developers. Protein Sci. *30*, 70–82.

Pfeiffer, K., Gohil, V., Stuart, R.A., Hunte, C., Brandt, U., Greenberg, M.L., and Schägger, H. (2003). Cardiolipin stabilizes respiratory chain supercomplexes. J. Biol. Chem. *278*, 52873–52880.

Punjani, A., Rubinstein, J.L., Fleet, D.J., and Brubaker, M.A. (2017). CryoSPARC: algorithms for rapid unsupervised cryo-EM structure determination. Nat. Methods *14*, 290–296.

Qin, L., Hiser, C., Mulichak, A., Garavito, R.M., and Ferguson-Miller, S. (2006). Identification of conserved lipid/detergent-binding sites in a high-resolution structure of the membrane protein cytochrome *c* oxidase. Proc. Natl. Acad. Sci. U S A *103*, 16117–16122.

Qin, L., Sharpe, M.A., Garavito, R.M., and Ferguson-Miller, S. (2007). Conserved lipid-binding sites in membrane proteins: a focus on cytochrome *c* oxidase. Curr. Opin. Struct. Biol. *17*, 444–450.

Rich, P.R. (2004). The quinone chemistry of *bc* complexes. Biochim. Biophys. Acta *1658*, 165–171.

Rubinstein, J.L., and Brubaker, M.A. (2015). Alignment of cryo-EM movies of individual particles by optimization of image translations. J. Struct. Biol. *192*, 188–195.

Sarewicz, M., and Osyczka, A. (2015). Electronic connection between the quinone and cytochrome *c* redox pools and its role in regulation of mitochondrial electron transport and redox signaling. Physiol. Rev. *95*, 219–243.

Sarewicz, M., Pintscher, S., Pietras, R., Borek, A., Bujnowicz, Ł., Hanke, G., Cramer, W.A., Finazzi, G., and Osyczka, A. (2021). Catalytic reactions and energy conservation in the cytochrome *bc*$_1$ and *b*$_6$*f* complexes of energy-transducing membranes. Chem. Rev. *121*, 2020–2108.

Schrödinger, L. (2015). The PyMOL Molecular Graphics System, Version 2.0 S (pymol.org).

Sharma, V., and Wikström, M. (2016). The role of the K-channel and the active-site tyrosine in the catalytic mechanism of cytochrome *c* oxidase. Biochim. Biophys. Acta *1857*, 1111–1115.

Smirnova, I.A., Ädelroth, P., Gennis, R.B., and Brzezinski, P. (1999). Aspartate-132 in cytochrome *c* oxidase from *Rhodobacter sphaeroides* is involved in a two-step proton transfer during oxo-ferryl formation. Biochemistry *38*, 6826–6833.

Sone, N., Nagata, K., Kojima, H., Tajima, J., Kodera, Y., Kanamaru, T., Noguchi, S., and Sakamoto, J. (2001). A novel hydrophobic diheme *c*-type cytochrome. Purification from *Corynebacterium glutamicum* and analysis of the QcrCBA operon encoding three subunit proteins of a putative cytochrome reductase complex. Biochim. Biophys. Acta *1503*, 279–290.

Stowell, M.H.B., McPhillips, T.M., Rees, D.C., Soltis, S.M., Abresch, E., and Feher, G. (1997). Light-induced structural changes in photosynthetic reaction center: implications for mechanism of electron-proton transfer. Science *276*, 812.

Sun, C., Benlekbir, S., Venkatakrishnan, P., Wang, Y., Hong, S., Hosler, J., Tajkhorshid, E., Rubinstein, J.L., and Gennis, R.B. (2018). Structure of the alternative complex III in a supercomplex with cytochrome oxidase. Nature *557*, 123–126.

Svensson-Ek, M., Abramson, J., Larsson, G., Törnroth, S., Brzezinski, P., and Iwata, S. (2002). The X-ray crystal structures of wild-type and EQ(I-286) mutant cytochrome c oxidases from rhodobacter sphaeroides. J. Mol. Biol. *321*, 329–339.

Di Trani, J.M., Liu, Z., Whitesell, L., Brzezinski, P., Cowen, L.E., and Rubinstein, J.L. (2021). Rieske head domain dynamics and indazole-derivative inhibition of *Candida albicans* complex III. Structure *S0969-2126*, 00301-4.

Tsukihara, T., Aoyama, H., Yamashita, E., Tomizaki, T., Yamaguchi, H., Shinzawa-Itoh, K., Nakashima, R., Yaono, R., and Yoshikawa, S. (1996). The whole structure of the 13-subunit oxidized cytochrome *c* oxidase at 2.8 Å. Science *272*, 1136–1144.

Unthan, S., Grünberger, A., van Ooyen, J., Gätgens, J., Heinrich, J., Paczia, N., Wiechert, W., Kohlheyer, D., and Noack, S. (2014). Beyond growth rate 0.6: what drives Corynebacterium glutamicum to higher growth rates in defined medium. Biotechnol. Bioeng. *111*, 359–371.

Wikström, M., Sharma, V., Kaila, V.R.I., Hosler, J.P., and Hummer, G. (2015). New perspectives on proton pumping in cellular respiration. Chem. Rev. *115*, 2196–2221.

Wikström, M., Krab, K., and Sharma, V. (2018). Oxygen activation and energy conservation by cytochrome *c* oxidase. Chem. Rev. *118*, 2469–2490.

Wiseman, B., Nitharwal, R.G., Fedotovskaya, O., Schäfer, J., Guo, H., Kuang, Q., Benlekbir, S., Sjöstrand, D., Ädelroth, P., Rubinstein, J.L., et al. (2018).

Structure of a functional obligate complex III_2IV_2 respiratory supercomplex from *Mycobacterium smegmatis*. Nat. Struct. Mol. Biol. *25*, 1128–1136.

Yanofsky, D.J., Di Trani, J.M., Król, S., Abdelaziz, R., Bueler, S.A., Imming, P., Brzezinski, P., and Rubinstein, J.L. (2021). Structure of mycobacterial $CIII_2CIV_2$ respiratory supercomplex bound to the tuberculosis drug candidate telacebec (Q203). eLife *10*, e71959.

Yoshikawa, S., and Shimada, A. (2015). Reaction mechanism of cytochrome *c* oxidase. Chem. Rev. *115*, 1936–1989.

Zelle, E., Pfelzer, N., Oldiges, M., Koch-Koerfges, A., Bott, M., Nöh, K., and Wiechert, W. (2021). An energetic profile of *Corynebacterium glutamicum* underpinned by measured biomass yield on ATP. Metab. Eng. *65*, 66–78.

Zhang, Z., Huang, L., Shulmeister, V.M., Chi, Y.I., Kim, K.K., Hung, L.W., Crofts, A.R., Berry, E.A., and Kim, S.H. (1998). Electron transfer by domain movement in cytochrome bc_1. Nature *392*, 677–684.

Zheng, S.Q., Palovcak, E., Armache, J.-P., Verba, K.A., Cheng, Y., and Agard, D.A. (2017). MotionCor2: anisotropic correction of beam-induced motion for improved cryo-electron microscopy. Nat. Methods *14*, 331–332.

STAR★METHODS

KEY RESOURCES TABLE

REAGENT or RESOURCE	SOURCE	IDENTIFIER
Chemicals, peptides, and recombinant proteins		
Protease inhibitor phenylmethanesulfonyl fluoride	Sigma	Cat#P7626
DNase I	Roche	Cat#10104159001
Strep-Tactin Superflow resin	Iba Lifescience	Cat# 2-1206-025
D-desthiobiotin	Iba Lifescience	Cat# 2-1000-001
n-dodecyl β-D-maltoside (DDM)	Glycon	Cat#D97002-C
Glyco-diosgenin (GDN)	Anatrace	Cat#GDN101
2,3-dimethyl-[1,4]naphthoquinone	Rare Chemicals GmbH	Cat#BWGA0196
Deposited data		
III_2IV_2 Supercomplex from *Corynebacterium glutamicum*, map	This paper	EMDB ID: EMD-13777
III_2IV_2 Supercomplex from *Corynebacterium glutamicum*, model	This paper	PDB ID: 7Q21
Experimental models: Organisms/strains		
Corynebacterium glutamicum, strain ΔC-D_{St} (13032ΔctaD with pJC1-ctaD$_{St}$)	(Niebisch and Bott, 2003)	N/A
Recombinant DNA		
pJC1-ctaD$_{St}$	(Niebisch and Bott, 2003)	N/A
Software and algorithms		
cryoSPARC ver. 2	(Punjani et al., 2017)	https://cryosparc.com/
Coot	(Emsley et al., 2010)	https://www2.mrc-lmb.cam.ac.uk/personal/pemsley/coot
Phenix	(Liebschner et al., 2019)	https://www.phenix-online.org/
UCSF ChimeraX	(Pettersen et al., 2021)	https://www.cgl.ucsf.edu/chimerax/
UCSF Chimera	(Pettersen et al., 2004)	https://www.cgl.ucsf.edu/chimera/
PyMOL	(Schrödinger, 2015)	https://pymol.org/2/
Other		
Superose 6 Increase 10/300 GL column	GE Healthcare	Cat#GE17-5172-01

RESOURCE AVAILABILITY

Lead contact

Further information and requests for resources and reagents should be directed to and will be fulfilled by the lead contact, Peter Brzezinski (peter.brzezinski@dbb.su.se).

Materials availability

This study did not generate new unique reagents.

Data and code availability

The atomic coordinates and the cryo-EM density maps from this study are available at the electron microscopy databank (https://www.ebi.ac.uk/pdbe/emdb) and protein databank (https://www.rcsb.org) under accession numbers EMD-13777, PDB: 7Q21.

This paper does not report original code.

Any additional information required to reanalyze the data reported in this paper is available from the lead contact upon request.

EXPERIMENTAL MODEL AND SUBJECT DETAILS

Corynebacterium glutamicum, strain ΔC-D_{St} (13032Δ*ctaD* with pJC1-*ctaD*$_{St}$), described before (Niebisch and Bott, 2003), was grown on BHI-Agar plates (33 g/l brain heart infusion broth, 15 g/l agar, 20 g/l D-(+)-glucose, 25 mg/l kanamycin). Single colonies were picked, inoculated into 10 ml BHI culture medium and grown over night using a shaker at 300 rpm, 30°C. The pre-culture was diluted into 500 ml CGXII medium (Unthan et al., 2014) in a 2 l flask and shaken at 160 rpm, 30°C until the OD_{600} reached 12. The cells were again diluted into 2 l CGXII medium in a 5 l baffled flask and shaken at 130 rpm, 30°C. The cells were harvested at OD_{600} 17, 10 000 x *g* for 30 min, JLA 8.1000 rotor (Beckman).

METHOD DETAILS

Membrane preparation

Cells were homogenized in 4 ml cell lysis buffer (100 mM Tris-HCl at pH 7.5, 5 mM $MgSO_4$) per gram of cells in the presence of 100 mg of a protease inhibitor phenylmethanesulfonyl fluoride (Sigma) and 10 mg DNaseI (Roche). Cells were broken with a cell disrupter with 4 cycles at 35 kPsi (Constant Systems) and cellular debris was removed by centrifugation at 90 000 x *g* for 20 min at 4°C (45 Ti rotor, Beckman). Membranes were collected by ultracentrifugation at 220 000 x *g* for 90 min at 4°C (45Ti rotor, Beckman).

Isolation of supercomplexes

Membranes were solubilized in 100 mM Tris-HCl pH 7.5, 100 mM NaCl, 2 mM $MgSO_4$, 50 mg/l avidin (to prevent unspecific binding to the column, see below), 1% (w/v) DDM to a protein concentration of 5 mg/ml and incubated for 45 min, at 4°C under gentle stirring. Insolubilized material was removed by ultracentrifugation at 39 000 x *g*, 20 min, 4°C (SW41 rotor, Beckman). The supernatant was concentrated with a 100-kDa molecular weight cutoff concentrator (Merck Millipore) until the volume was reduced to 5 ml. The concentrated supernatant was then diluted in solubilization buffer without detergent to yield a final DDM concentration of 0.1 % (w/v) and concentrated again to reach a volume of <10 ml. The concentrated supernatant was applied to a gravity flow Strep-Tactin Superflow column (4 ml bed volume, Iba Lifescience). The column was washed 3 times with 0.5 column volumes of washing buffer (100 mM Tris-HCl pH 7.5, 100 mM NaCl, 2 mM $MgSO_4$, 0.05% (w/v) DDM). The protein was then eluted with 3 column volumes of elution buffer (100 mM Tris-HCl pH 7.5, 100 mM NaCl, 2 mM $MgSO_4$, 0.05 % (w/v) DDM, 2.5 mM D-desthiobiotin). The eluted supercomplex solution was concentrated as described above and further purified by size exclusion chromatography on a Superose 6 Increase 10/300 GL column (GE Healthcare), pre-equilibrated with buffer (100 mM Tris-HCl pH 7.5, 100 mM NaCl, 2 mM $MgSO_4$, 0.05 % DDM) using an Äkta Pure M25 chromatography system (GE Healthcare) operated at 4°C with UV detection at 280 nm and 415 nm. Collected fractions containing supercomplex were concentrated for further analysis.

Spectral analysis

The purified supercomplex was analyzed by UV–visible absorption spectroscopy (Cary 100 Spectrophotometer, Agilent Technologies). Difference spectra of the dithionite-reduced and oxidized states of the supercomplex were recorded. The reduced - oxidized difference absorption coefficients used to estimate the cofactor stoichiometry were: $\varepsilon_{605-630}$ = 24 mM^{-1} cm^{-1} (cyt. aa_3), $\varepsilon_{562-577}$ = 22 mM^{-1} cm^{-1} (cyt. *b*), and $\varepsilon_{552-540}$ = 19 mM^{-1} cm^{-1} (cyt. *c*) (Megehee et al., 2006; Niebisch and Bott, 2003).

Preparation of menaquinol

2,3-dimethyl-[1,4]naphthoquinone (Rare Chemicals GmbH) was dissolved in ethanol (1.8 mg in 0.5 ml) to yield a 20 mM solution. Several crystals of sodium borohydride ($NaBH_4$) were added to reduce the quinone to quinol. The solution was kept on ice until transparent and HCl was added until formation of small bubbles in the solution ended. The sample was centrifuged for 10 min at 10 000 x *g* and the supernatant containing reduced quinol was aliquoted, flash frozen, and stored in −80°C until use.

Activity assays

The O_2 reduction rate was measured at 25°C using a Clark-type oxygen electrode in a buffer containing 100 mM Tris-HCl pH 7.5, 100 mM NaCl, 2 mM $MgSO_4$, 0.05 % DDM. The reaction was initiated by addition of 5 µl of 20 mM 2,3-dimethyl-[1,4]naphthoquinol solution into a 1 ml chamber containing the supercomplex solution (40 nM). The activity was obtained from the initial slope of the graph. The background O_2-reduction rate was measured and subtracted from the O_2-reduction rate obtained in the presence of the supercomplex.

Gel electrophoresis

Blue Native (BN) PAGE was performed according to the manufacturer's instruction with pre-cast gel, NativePAGE™ 4-16 % Bis-Tris (Thermo Fisher Scientific). The gel was run at 4°C for 60 min at 150 V, then the cathode buffer was exchanged to anode buffer and run for an additional 40 min at 250 V. The gel was then stained with Coomassie Brilliant Blue. The band corresponding to supercomplex from BN PAGE was subjected to mass spectrometry (LC-MS/MS), using digestion with trypsin and a 35 min gradient, which indicated the presence of both complexes III_2 and IV, as well as two additional subunits, LpqE and AscA (P20, PRSAF1). AscB and AscC were not identified in the mass spectrometric analysis of BN PAGE.

SDS PAGE was performed according to manufacturer's instruction with pre-cast gel, NuPAGE ^{TM} 4-12% Bis-Tris (Thermo Fisher Scientific) in MES running buffer. Samples were heated at 65°C for 30 min and run at 4°C for 45 min at 200 V. The gel was then stained with Coomassie Brilliant Blue. Bands assigned to four accessory subunits were subjected to mass spectrometry as described above (see Figure S1D). CtaF, AscA, AscC and Cg1128 were identified in the mass spectrometric analysis of SDS PAGE.

Grid preparation and cryo-electron microscopy

Purified supercomplexes (3 μl) at a concentration of 10 mg ml^{-1} was applied to holey carbon film coated copper EM grids (C flat 2/2 3C T50) that had been glow-discharged in air for 120 s at 20 mA (PELCO easiGlow). Grids were blotted for 3 s at 4°C and 100% humidity before being plunge-frozen in liquid ethane with a Vitrobot Mark IV (Thermo Fisher Scientific). Cryo-EM images were collected at 300 kV with a Titan Krios electron microscope (Thermo Fisher Scientific) equipped with a Gatan K2-summit direct electron detector and a Bio-quantum energy filter (Gatan). Data were collected with a nominal magnification of 130 000 x, corresponding to a calibrated pixel size of 1.06 Å. Automated data collection was done with the EPU software package (Thermo Fisher Scientific). A dataset of 2768 movies was collected, each consisting of 40 exposure fractions. The camera exposure rate and the total exposure of the specimen were 7.7 e^{-}/pixel/s and 55 e^{-}/Å^2, respectively (Table S3).

Image analysis

All image analysis was performed with cryoSPARC v2 unless otherwise stated (Punjani et al., 2017). Movies were aligned with *MotionCor2* (Zheng et al., 2017) and contrast transfer function (CTF) parameters were estimated in patches. Templates for particle selection were generated by 2D classification of manually selected particle images. A total of ~560 000 particle images were selected, images were corrected for local motion (Rubinstein and Brubaker, 2015) and extracted in 310 × 310 pixel boxes. The dataset was first cleaned with 2D classification and then with three rounds of *ab initio* 3D classification and heterogeneous refinement reducing the size to ~65 000 particle images. Local and global CTF refinement followed by homogeneous refinement without the application of symmetry resulted in a map at 2.9 Å resolution.

Figures were prepared using the software PyMOL (Molecular Graphics System, Version 2.0 Schrödinger, LLC., (Schrödinger, 2015)) as well as UCSF ChimeraX (Pettersen et al., 2021) and Chimera (Pettersen et al., 2004). developed by the Resource for Biocomputing, Visualization, and Informatics at the University of California, San Francisco, with support from NIH P41-GM103311.

Model building and refinement

An initial model of all the subunits of the *C. glutamicum* supercomplex was built manually into the C1 symmetry density map with 2.9 Å resolution using Coot (Emsley et al., 2010). Subunits AscB, AscC, AscD and AscE were initially build as a poly-alanine chains. Sequences of AscB and AscC were then built into the density map where high enough resolution allowed identification of amino-acid side chains, based on known sequences of the *C. glutamicum* genome using BLAST (Altschul et al., 1990). No sequence match was found for AscD; it remained modelled as a poly-alanine chain. The model was refined using combination of phenix_real_space_refine (Afonine et al., 2018) and manual adjustments in Coot (Liebschner et al., 2019).

QUANTIFICATION AND STATISTICAL ANALYSIS

Data from the MQH_2:O_2 oxidoreductase activity assay are presented as mean +/− standard error of the mean from 4 technical replicates. The values are reported in the text and details are found in the methods description.